Néel Vector Induced Manipulation of Valence States in the Collinear Antiferromagnet Mn_2Au

H.J. Elmers,[*,†] S.V. Chernov,[†] S. W. Dsouza,[‡] S.P. Bommanaboyena,[†] S.Yu. Bodnar,[†] K. Medjanik,[†] S. Babenkov,[†] O. Fedchenko,[†] D. Vasilyev,[†] S. Y. Agustsson,[†] C. Schlueter,[¶] A. Gloskovskii,[¶] Yu. Matveyev,[¶] V. N. Strocov,[§] Y. Skourski,[‖] L. Šmejkal,[†] J. Sinova,[†] J. Minár,[‡] M. Kläui,[†] G. Schönhense,[†] and M. Jourdan[†]

[†]*Institut für Physik, Johannes Gutenberg-Universität, Staudingerweg 7, D-55099 Mainz, Germany*

[‡]*New Technologies-Research Centre, University of West Bohemia, Univerzitni 8, 306 14 Pilsen, Czech Republic*

[¶]*Deutsches Elektronen-Synchrotron DESY, 22607 Hamburg, Germany*

[§]*Swiss Light Source, Paul Scherrer Institut, CH-5232 Villigen-PSI, Switzerland*

[‖]*Dresden High Magnetic Field Laboratory (HLD-EMFL), Helmholtz-Zentrum Dresden-Rossendorf, 01328 Dresden, Germany*

E-mail: elmers@uni-mainz.de

Abstract

The coupling of real and momentum space is utilized to tailor electronic properties of the collinear metallic antiferromagnet Mn_2Au by aligning the real space Néel vector indicating the direction of the staggered magnetization. Pulsed magnetic fields of 60 T were used to orient the sublattice magnetizations of capped epitaxial $Mn_2Au(001)$ thin

films perpendicular to the applied field direction by a spin-flop transition. The electronic structure and its corresponding changes were investigated by angular-resolved photoemission spectroscopy with photon energies in the vacuum-ultraviolet, soft and hard X-ray range. The results reveal an energetic rearrangement of conduction electrons propagating perpendicular to the Néel vector. They confirm previous predictions on the origin of the Néel spin-orbit torque and anisotropic magnetoresistance in Mn_2Au, and reflect the combined antiferromagnetic and spin-orbit interaction in this compound leading to inversion symmetry breaking.

Keywords

antiferromagnetism, topology, electronic structure, momentum microscopy, photoemission, harpes, arpes

The alignment of the staggered magnetization of collinear antiferromagnets, defined as the Néel vector, has been proposed to encode information in analogy to the magnetization vector in ferromagnets.[1] Information can be stored for example in an antiferromagnet-based tunnel junction.[2] The Néel vector orientation is robust against external magnetic fields and is expected to enable writing processes, which can be three orders of magnitude faster than those based on the magnetization vector of ferromagnets.[3] These intriguing properties initiated the field of antiferromagnetic spintronics,[4–6] which requires alternative means for the manipulation of the Néel vector. A promising pathway is based on Néel spin-orbit torques (NSOTs), which correspond to a staggered effective field generated by an electric current in the bulk of metallic antiferromagnets with a specific symmetry of the crystal lattice and strong spin-orbit interactions.[7] Up to now, electrical current induced manipulation of the Néel vector based on this mechanism was demonstrated for only two metallic compounds: CuMnAs[8–10] and Mn_2Au.[11–15] In principle, also non-NSOT related mechanisms can result in current induced resistance modifications.

In antiferromagnetic spintronics, efficient read-out of the Néel vector orientation poses a challenge for applications. In this framework, anisotropic magnetoresistance (AMR) potentially provides a simple read-out mechanism. However, this is typically an effect smaller than 1 %.[16] In the case of $Mn_2Au(001)$, recent experiments showed an AMR of about 0.15 %.[17] However, most applications require magnetoresistances above 20 %.[18]

A large Néel spin-orbit torque as well as a large AMR originate in the electronic band dispersion close to the Fermi energy. Such changes of the band structure of Mn_2Au at certain hot spots below the Fermi energy in reciprocal space have actually been predicted by theory.[7,11] In general, modifications of the band structure due to antiferromagnetic as well as ferromagnetic order are conventionally considered to be small, but cause macroscopic and application-relevant effects. These macroscopic effects include the intrinsic anomalous Hall effect,[19,20] the AMR,[21] and the magnetocrystalline anisotropy.[22]

For ferromagnets, variations of electronic states due to reorientation of the magneti-

zation direction have been observed using high-resolution angular-resolved photoemission spectroscopy (ARPES).[23]

In this work, spin-orbit-induced lifting of degeneracies was observed for the ferromagnetic material Fe. Similar effects occur in $EuIr_2Si_2$ due to an interaction of the Rashba effect with emergent two-dimensional ferromagnetism at the surface of this compound.[24]

In the case of antiferromagnets, one wants to understand, if a real space reorientation of the antiferromagnetic order parameter causes significant changes in momentum space, which for specific materials are predicted to allow for the occurrence of metal-insulator transitions and Dirac quasiparticles.[25] Antiferromagnets are more favorable for these concepts because of their symmetric spin-dependent density of states in contrast to ferromagnets. Therefore, k-resolved experimental investigations of the dependence of electronic states of antiferromagnets on the real space order parameter are required.

We demonstrate considerable Néel vector alignment induced changes of the electronic band dispersion close to the Fermi energy of epitaxial $Mn_2Au(001)$ films using the recently established method of bulk sensitive hard X-ray angular resolved photoemission spectroscopy (HARPES)[26,27] as well as more surface sensitive soft X-ray (SX-)ARPES.

RESULTS AND DISCUSSIONS

Epitaxial $Mn_2Au(001)$ films with a thickness of 40 nm were grown by rf-sputtering on $Al_2O_3(1\bar{1}02)$ substrates with a Ta buffer. The films were capped by ≈ 2 nm protective coating consisting of either Ta, AlO_x, or SiN to allow for ambient air transport. The samples were characterized by X-ray and electron diffraction as well as by atomic force microscopy (see section METHODS and Refs.[28,29]). During growth, the magnetic in-plane anisotropy aligns the Néel vector equally distributed along both magnetic easy axes [110] and $[1\bar{1}0]$ with magnetic domains of an average diameter of 1 μm.[30] Mn_2Au possesses a body centered tetragonal crystal structure (bct_2), where the (001) plane shows a 4-fold structural symmetry.

Because the photoemission experiment averages over many magnetic domains, it is not possible to observe Néel vector induced deviations from the 4-fold symmetry without large-scale aligning of the Néel vector along one easy axis. This was achieved by a spin-flop transition induced *ex situ* in a pulsed magnetic field of 60 Tesla prior to the photoemission experiment, resulting in a remanent orientation of the Néel vector perpendicular to the applied magnetic field.[31]

We performed ARPES in the hard and soft X-ray regime on these samples. The high photon energy $\approx$ 5 keV in HARPES results in correspondingly high kinetic energies of the photoemitted electrons. Their inelastic mean free path of $\approx$ 5 nm[32] allows to acquire momentum-resolved photoemission data from the bulk of the epitaxial film through the amorphous capping layer. Also SX-ARPES is possible through a capping layer and enables a higher energy and momentum resolution. However, the lower soft X-ray photon energy of $h\nu \simeq 800$ eV corresponds to a reduced inelastic mean free path of $\approx$ 1 nm,[32] which is associated with a reduced bulk sensitivity.

Fig. 1 shows a schematic sketch of the geometry of the HARPES experiment. The Néel vector is either oriented along the k_x or along the k_y direction, corresponding to an easy $< 110 >$ direction, as indicated by the green/red arrows on the samples surface and the blue/red arrows in the unit cell. The spin-flop generating field pulse defines an axis perpendicular to which the Néel vector is aligned. Thus, the formation of 180 degree AFM domains with the Néel vector aligned in opposite directions perpendicular to the field pulse is to be expected, which is consistent with our previous X-ray magnetic linear dichroism photoemission electron microscopy (XMLD-PEEM) investigations.[30]

As we will discuss in more detail in section DISCUSSION, in Mn_2Au the crystallographic inversion symmetry is broken by the antiferromagnetic order. This means that for the comparison of band structure calculations with the experimental HARPES data, averaging over both opposite directions of the Néel vector associated with the field induced alignment has to be considered. Even after this, as shown in Fig. 1, calculated constant energy cuts

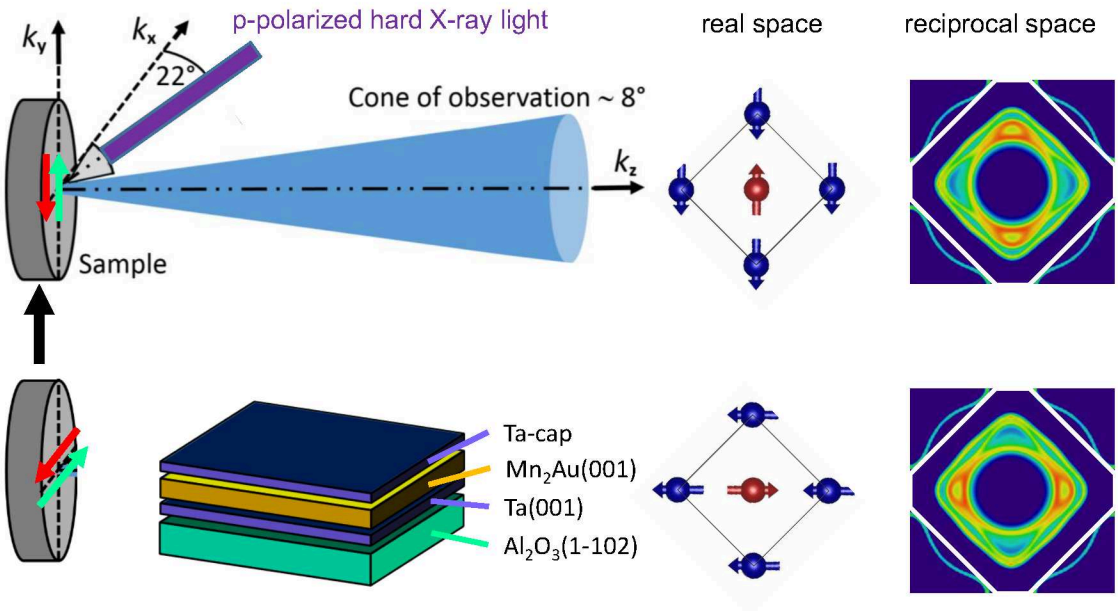

Figure 1: Sketch of the experiment defining the geometry for the HARPES experiment. Red/green arrows on the sample surface and red/blue arrows in the real space unit cells indicate the field-aligned Néel vector pointing parallel to the k_x and k_y axis, respectively. Calculated k_x-k_y momentum patterns at $E_B = 0.25$ eV predicting significant asymmetries of the spectral function associated with the Néel vector orientation (color code, see Fig. 2).

of the band structure show the Néel vector orientation dependent spin-orbit interaction in reciprocal space by breaking the 4-fold crystallographic symmetry of the $Mn_2Au(001)$ plane.

Photoemitted electrons carrying the momentum information from initial band states of Mn_2Au are augmented by electrons that have lost their momentum specificity due to the relaxation of the momentum conservation at the lattice distorted by atomic thermal motion. Both groups of electrons are subject to electron diffraction that modulates the observed intensity. Using the XPD removal procedure described in Ref.[27] and subtracting a constant background signal, one obtains the band dispersion in the valence band range. Fig. 2 shows the photoemission results obtained for a photon energy of $h\nu = 5230$ eV within an acquisition time of 12 hours. To further increase the statistical significance, the signal from four simultaneously acquired Brillouin zones have been averaged. Furthermore, the photoemission intensities have been symmetrized according to $I(k_x) = I(-k_x)$ and $I(k_y) = I(-k_y)$.

The photon energy has been chosen to adjust the perpendicular momentum component $k_\perp$ to the center of one Brillouin zone. Assuming direct transitions into quasi-free-electron-like final states,[34,35] we calculate the absolute value of the final state momentum by the dispersion relation

$$k_{\text{final}} = (1/\hbar)\sqrt{2m_{eff}E_{\text{final}}}; \quad E_{\text{final}} = h\nu - E_B + V_0^*, \tag{1}$$

where m_{eff} denotes the effective electron mass, $h\nu$ the photon energy, E_B the binding energy and V_0 the inner potential with respect to the Fermi energy. Considering just the transition in periodic k-space, we disregard the surface, the work function, diffraction effects at the surface (surface Umklapp) and the refraction of the outgoing electron wave at the surface barrier. This is justified because of the high kinetic energy of the final states.

In comparison to the large final state momentum, the changes with increasing binding energy according to Eq. 1 as well as the curvature of the final-state sphere are small. Therefore,

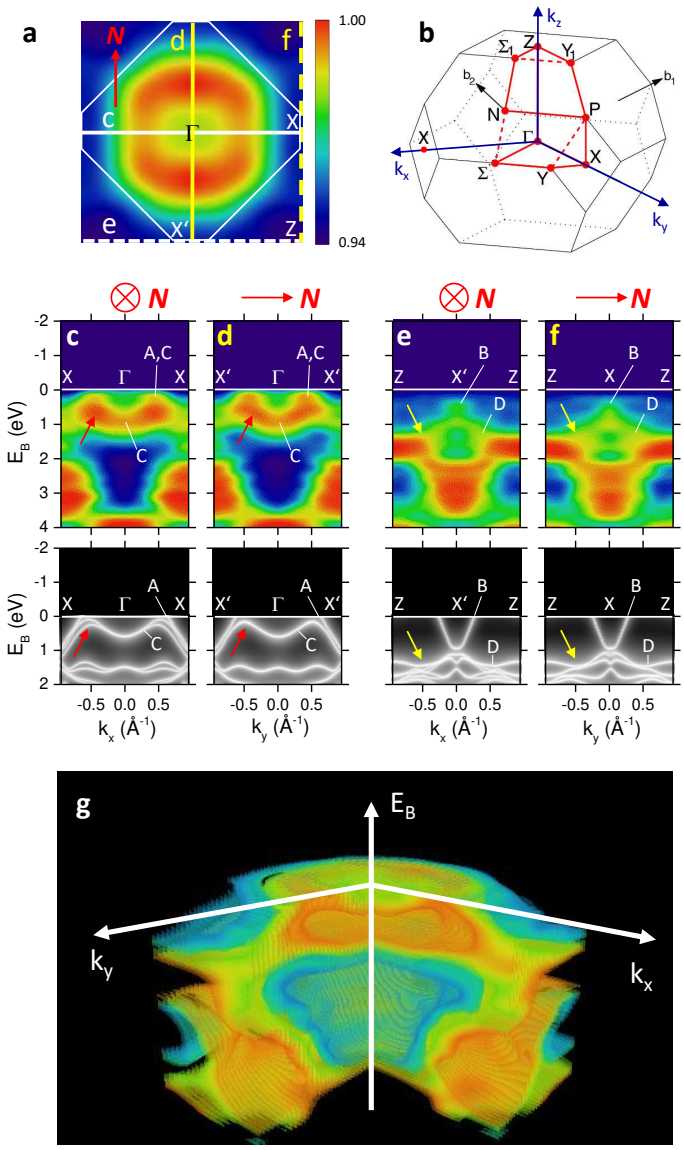

Figure 2: **a** Constant energy section at the Fermi energy of the photoemission intensity $I(E_F, k_x, k_y)$ measured for an excitation energy of 5230 eV, corresponding to a cut through the Fermi surface in the Γ-X-Σ plane with indicated orientation of the Néel vector $\boldsymbol{N}$. The color code for the intensity is indicated by the color bar on the right. **b** First Brillouin zone of the body centred tetragonal (bct_2) structure of Mn_2Au based on Ref.[33] **c** Band dispersion $I(E_B, k_x, k_y = 0)$ along X-Γ-X indicated by the full white line in **a**. The corresponding calculated band dispersion is shown below using a black/white color code with white indicating high spectral density. The letters A-D are used to label the different bands. **d** Band dispersion $I(E_B, k_x = 0, k_y)$ along X'-Γ-X' indicated by the full yellow line in **a** and corresponding theoretical result below. **e,f** Similar data along Z-X'-Z and Z-X-Z parallel to k_x and k_y indicated by the broken white and yellow lines at the rim of **a** and corresponding theory results below. **g** Three-dimensional visualization of the measured intensity array $I(E_B, k_x, k_y)$.

the photon energy of 5230 eV approximately probes the Γ-X-Σ plane [see Fig. 2 **b**].

Fig. 2 **a** shows the constant energy section of the photoemission intensity at the Fermi energy, $I(E_B = E_F, k_x, k_y, k_z = 0)$, being equivalent to an almost planar cut through the Fermi surface in the Γ-X-Σ plane. Fig. 2 **a** covers the full centred Brillouin zone, where Z-points form the edges of the depicted section. The ring-shaped feature indicates the Fermi surface in the Γ-X-Σ plane.

E_B *versus* $k_\parallel$ sections along the X-Γ-X, and Z-X-Z lines parallel to k_x [Fig. 2 **c,d**] and k_y [Fig. 2 **e,f**] reveal the band dispersions. The finite energy (170 meV) and momentum resolution (0.3 Å^{-1}), which is caused by the photon bandwidth of the beamline and by the sample properties (see Methods), respectively, causes a Gaussian blurring of the bands. Calculated band dispersions (see Methods section), averaging both antiparallel orientations of the Néel vector parallel to k_x and k_y ([110] and [1-10]), corresponding to the experimental configuration, are shown in the lower row. The agreement of the positions with maximum intensity/ spectral weight and specifically the associated symmetry breaking induced by the alignment of the Néel vector is relatively good close to the Fermi energy. However, at increased binding energies the differences become more obvious as the experimentally observed intensity moves in contrast to the calculations of the spectral function more towards the Γ-point, which is due to an increased value of the photoemission matrix element for the band C minimum.

The Fermi surface originates from an inverted (hole-like) parabolic band A with the apex lying above the Fermi level as shown in Fig. 2 **c,d**. A second band C occurs just below band A close to the X point and disperses to larger binding energy upon approaching the Γ point, forming maxima near $k_x = \pm 0.5$ Å^{-1} and a minimum at the Γ point. Close to the X points, bands A and C are hardly resolved. The central minimum of band C that occurs in the theoretical result at $E_B = 0.5$ eV lies at $E_B = 0.9$ eV in the experiment, indicates a 400 meV shift to a higher binding energy. The difference can be attributed to electron correlation effects, which are not considered by the present calculation. The energy

broadening of bands A and C observed in the experiment near $k_x = \pm 0.5$ Å^{-1} results from the separation of these two bands, just before band A becomes unoccupied and therefore invisible for $|k_x| < 0.5$ Å^{-1}.

Most importantly, the band dispersions along k_x and k_y shown in Fig. 2 **c,d** deviate from each other. In the experiment, we observe a broader intensity maximum at $E_B = 0.7$ eV and $k_x = \pm 0.4$ Å^{-1} for the dispersion along k_x compared to the corresponding dispersion along k_y (indicated by the red arrow). This difference directly corresponds to the difference of the band dispersions in the theoretical results. The calculated band C splits near $k_x = \pm 0.5$ Å^{-1} for the case of the Néel vector aligned perpendicular to the dispersion direction. In contrast, band C appears degenerate for the Néel vectors pointing parallel to the dispersion direction.

A similar difference can be observed for E_B *versus* $k_{\|}$ sections along the Z-X-Z cuts parallel to k_x and k_y [Fig. 2 **e,f**]. Near the Z point one observes band D in the experimental data with small dispersion occurring at $E_B = 1.7$ eV. Whereas band D reveals a kink indicated by the yellow arrow at $k_x = \pm 0.5$ Å^{-1}, it shows a round shape in Fig. 2 **f** near $k_y = \pm 0.5$ Å^{-1}. Band D corresponds to the weakly dispersing band at $E_B = 1.3$ eV showing up in the calculated data. Near $k_x = \pm 0.5$ Å^{-1} band D splits for Néel vectors pointing perpendicular to the dispersion direction, whereas it appears degenerate for parallel Néel vectors and dispersion direction. This energy splitting lifts one of the partial bands and causes the increased photoemission intensity at $k_x = \pm 0.5$ Å^{-1} and $E_B = 1.5$ eV indicated by the arrows in Fig. 2 **e,f**.

A band gap opening occurs at the X-point between bands B and D. The cut along Z-X'-Z [Fig. 2 **e**] reveals the parabolic band B with the X-point apex at $E_B = 0.5$ eV. Band B with an inverted parabolic behavior is split off from band D by a band gap of 200 meV [Fig. 2 **e**]. This band gap is closed for the Néel vectors aligned parallel to the dispersion direction as shown in the Z-X-Z cut [Fig. 2 **f**]. The dependence of the band gap on the order parameter is also visible in the theoretical data. In the calculation, the band gap occurs at a higher binding energy of $E_B = 1$ eV. The decreased photoemission intensity for $E_B < 2$ eV near

the X-point is likely due to a Laue-type interference in photoemission.[36]

To exclude asymmetries resulting from linear dichroism in the angular distribution of the photoemission intensity and from substrate-induced asymmetries, such as surfaces with a small miscut, we performed experiments on a single sample, which was broken in two halves. After the separate Néel vector alignment by spin-flop of each half along perpendicular easy axis directions the halves were reunited on the sample holder and the photoemission experiment was performed in the same geometry for both halves by just lateral shifting the sample holder.

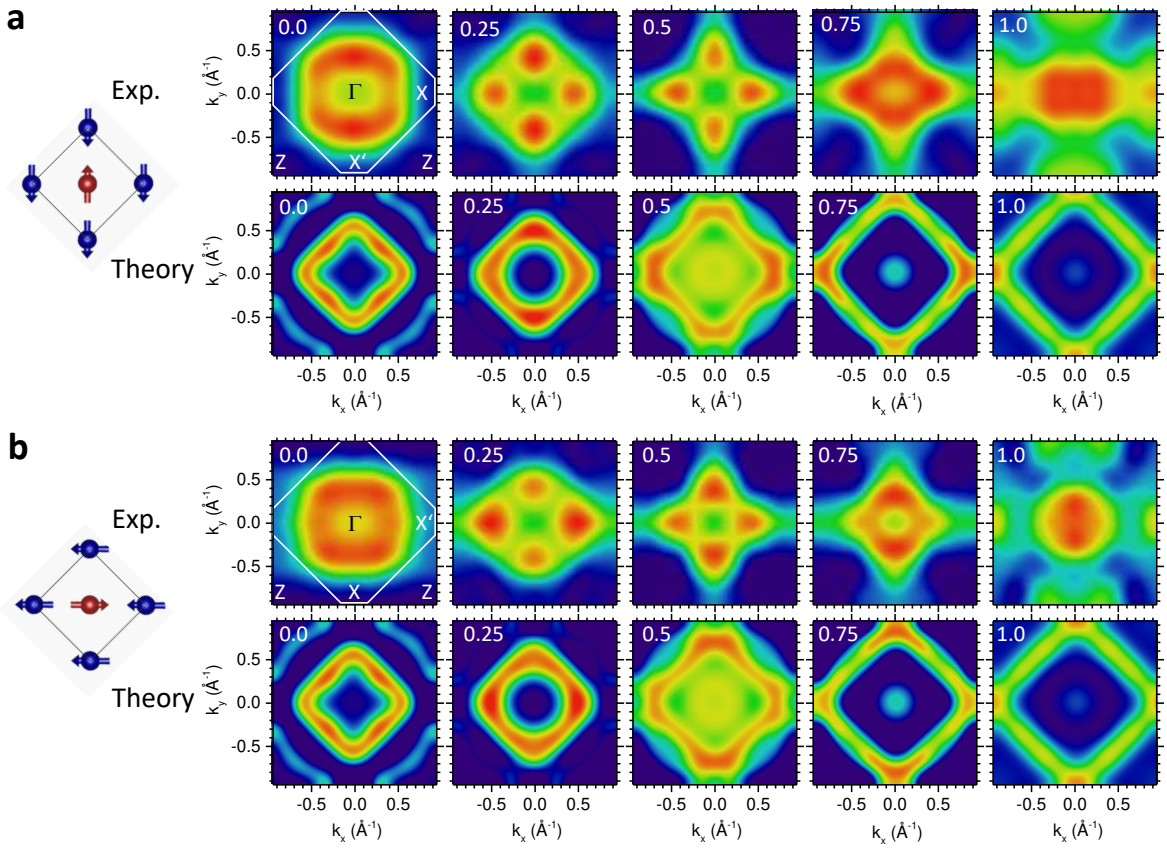

Figure 3: Upper rows: Photoemission results for two sample halves **a** and **b** measured in the same geometry with Néel vector alignment indicated on the real space unit cells on the left. Photoemission intensities represented as constant energy sections $I(E_B, k_x, k_y)$ at binding energies (in eV) given in the panels. The photon energy is 5230 eV. Lower rows show corresponding calculated spectral function densities. Color scale see Fig. 2 **a**.

Fig. 3 **a,b** compares details of the band dispersion as a sequence of constant energy

cuts for selected binding energies for both halves of the sample. The two-fold symmetric patterns in each series appear approximately rotated by 90 °. As the only difference of the investigated sample spots is the direction of the Néel vector alignment prior to the experiment, we conclude that the rotated photoemission intensity distribution with two-fold symmetry is associated with the symmetry breaking by the alignment direction of the Néel vector. Note that independent from this alignment of the Néel vector also the direction of incidence of the X-rays in the photoemission experiments breaks the 4-fold crystallographic symmetry of the $Mn_2Au(001)$ surface. However, the two-fold symmetry generated by this effect is identical for both halves of the investigated sample.

For comparison, the 2nd and 4th rows of Fig. 3 show *ab initio* calculations of the spectral function. The limited resolution of the experiment is accounted for by a Gaussian blur with a width of 150 meV. For HARPES the spectral function describes the essential physics of the photoemission process, as due to the high photon energies the influence of the final states in the photoexcitation process on the obtained photoemission intensities is weak for bands having the same atomic character and thus atomic cross-sections. In our case, though, all bands above $E_B = 2$ eV are mostly Mn derived, and this approximation holds. However, the variation of spectral intensities observed in the experiment can differ from the calculated spectral densities because the photoemission matrix elements depends on the band symmetries.

The experimental data at a binding energy of 0.25 eV reveal a larger intensity at $k_x = 0, k_y = \pm 0.5$ Å^{-1} as compared to $k_x = \pm 0.5$ Å^{-1}, $k_y = 0$. This observation agrees one-to-one with the theoretical prediction. The observed increased intensity along k_y at $E_B = 0.25$ eV results from the non-degenerate band C, the maximum of which is just touched by the constant energy cut in this direction. The lifted degeneracy of C along k_x distributes the spectral weight on a larger area, which decreases its maximum intensity. At binding energies of $E_B = 0.75$ eV and 1.0 eV the intensity appears larger along the k_x direction perpendicular to the alignment axis of the Néel vector. This is a consequence of touching the split branch

of band C with larger binding energy near the Γ point and the split branch with smaller binding energy near the X point.

For the sample half with 90° rotated Néel vector alignment, we observed basically the same intensity patterns, but rotated by 90°. We did not change anything apart from the direction of the spin-flop generating field pulse prior to the photoemission experiment. Thus, these results confirm the purely magnetic origin of the breaking of the four-fold crystal symmetry.

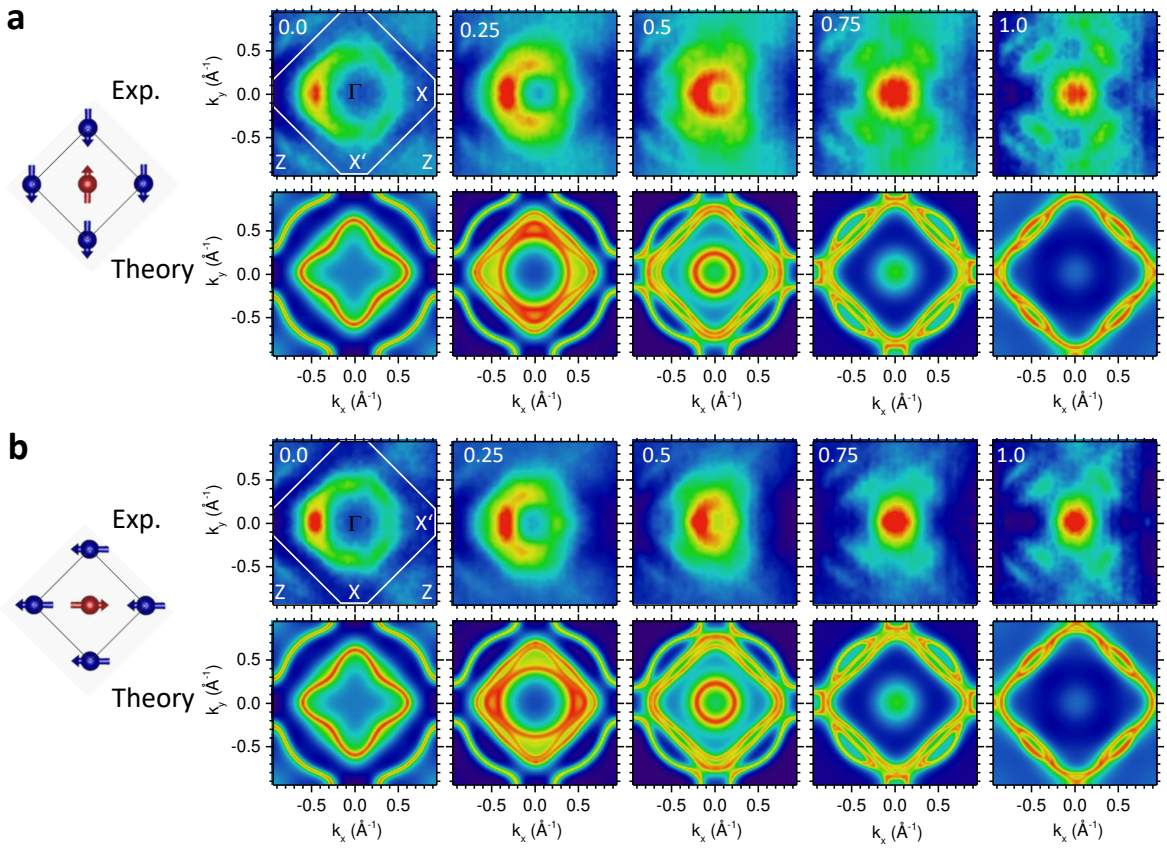

Figure 4: Upper rows: Soft X-ray photoemission results for two samples **a** and **b** measured in the same geometry with Néel vector alignment indicated on the real space unit cells on the left. Photoemission intensities represented as constant energy sections $I(E_B, k_x, k_y)$ at binding energies (in eV) given in the panels. The photon energy is 817 eV. The lower rows show corresponding calculated spectral function densities. Color scale see Fig. 2 **a**.

In order to improve the energy and momentum resolution, we performed a similar experiment using *p*-polarized soft X-ray excitation. For these measurements we used two

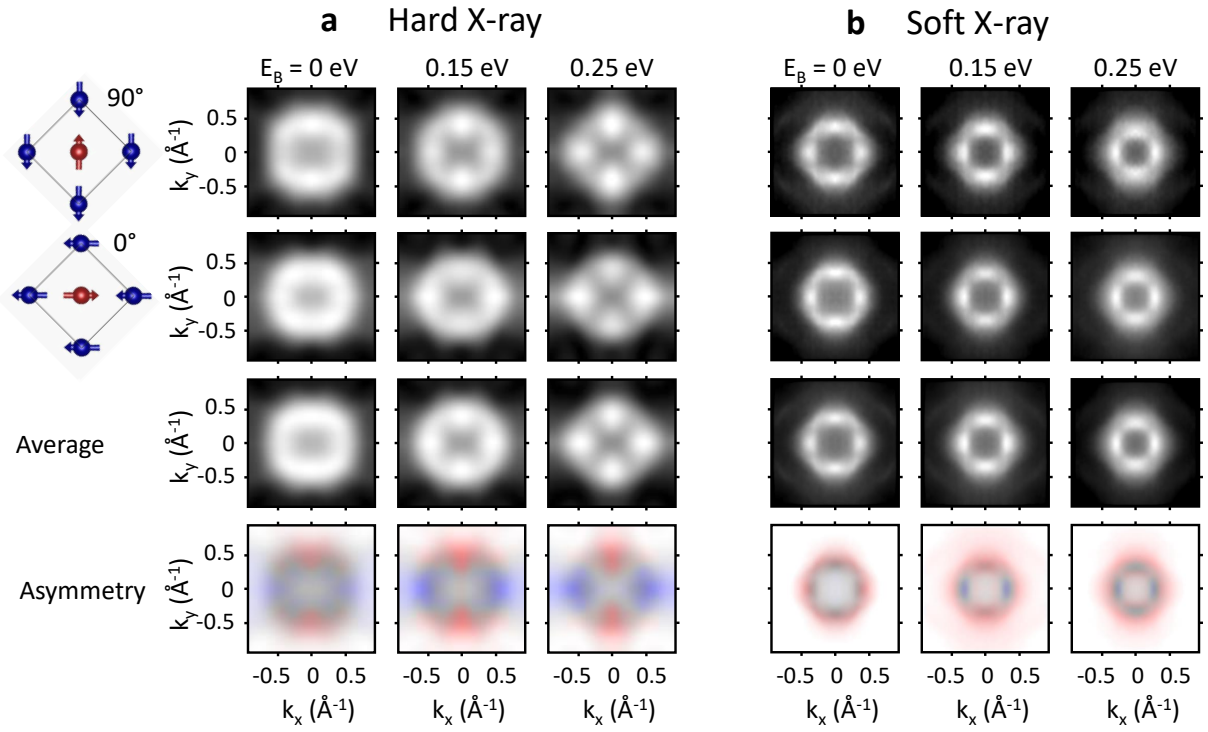

Figure 5: **a** Constant energy sections $I(E_B, k_x, k_y)$ at three distinct binding energies measured at a photon energy of 5230 eV for the two Néel vector alignments, mean intensity values and intensity asymmetries. The asymmetry images are plotted in the HSV (hue, saturation, value) representation, where the colors red and blue indicate the sign of the asymmetry, their color saturation the asymmetry value with a maximum of 10 %, and the color value the photoemission intensity. **b** Analogous data measured at a photon energy of 817 eV. The data is left/right symmetrized to eliminate the linear dichroism stemming from the illumination geometry.

Néel vector aligned Mn_2Au films capped by 2 nm SiN, using angular-resolved photoemission spectroscopy at a photon energy of 817 eV. The constant energy sections shown in Fig. 4 correspond to cuts through the center of the Brillouin zone similar to the sections shown in Fig. 3. The constant energy sections appear with larger momentum resolution. The illumination geometry causes a pronounced linear dichroism, *i.e.* left/right intensity asymmetry. The photoemission intensity agrees with the calculated spectral function density near the Fermi energy. More details of calculated bands A and C can be identified in the experimental data. Similar to the HARPES results, the binding energy of band C at Γ is larger in experiment resulting in the high intensity near Γ for $E_B = 0.75$ and 1.0 eV, which is absent in the calculated data because of the lower theoretical binding energy of band C.

To quantify the intensity asymmetry for the two Néel vector orientations, Fig. 5 **a** shows $k_x - k_y$ resolved intensity patterns at three distinct binding energies for both orientations, their mean value indicating the expected result for non-aligned Néel vector orientation. The intensity asymmetry is calculated according to $A = (I^{90} - I^0)/(I^{90} + I^0)$ with I^{90} and I^0 denoting the intensities (after background subtraction) measured for the two Néel vector orientations shown in the first and second row in Fig. 5. We observe a variation of the Néel vector alignment induced intensity asymmetry, which varies with the binding energy and is largest at $E_b \simeq 0.15$ eV with a maximum of 10 %. Fig. 5 **b** shows similar data obtained for soft X-ray excitation. In this case, the maximum intensity asymmetry observed at $E_B = 0.15$ eV is smaller (5 %) compared to the HARPES experiment. This smaller intensity asymmetry might be explained by a reduced magnetic order at the SiN/Mn_2Au interface, considering the reduced inelastic mean free path for the smaller photon energy. Qualitatively, the observed intensity asymmetry of both samples for soft X-ray excitation is the same as discussed above for the higher photon energy. Thus, these more surface sensitive results confirm the magnetically induced band structure variations observed by HARPES.

To further increase the energy and momentum resolution, we performed vacuum-ultraviolet (VUV-)ARPES using uncapped samples transferred in UHV between deposition chamber

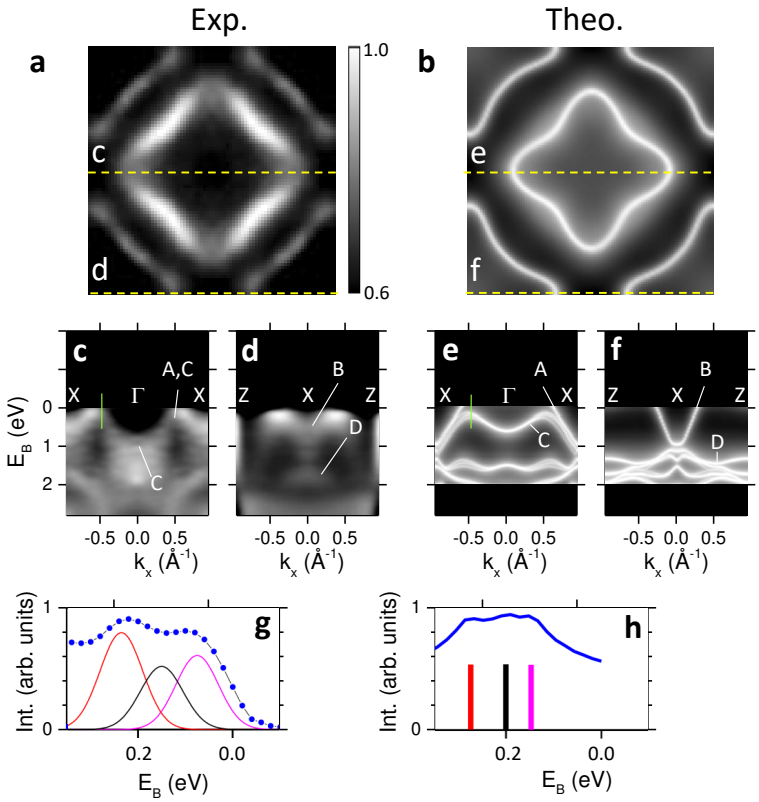

Figure 6: **a,c,d** Analogous data as shown in Fig. 2 but measured at a photon energy of 21.2 eV for uncapped films without Néel vector alignment. The calculated band structure **b,e,f** has been averaged to account for the as grown magnetic structure of the sample. **g,h** Energy distribution curves along the green profiles indicated in **c** and **e**.

and photemission set-up. Fig. 6 shows results obtained for excitation with 21.2 eV photons on a clean $Mn_2Au(001)$ film surface. For these uncapped samples, the Néel vector could not be aligned and the measurement averages over domains with the Néel vector directing along [110] and $[1\bar{1}0]$ (and the corresponding antiparallel directions). The energy resolution of this experiment (50 meV) enables a direct observation of the Néel vector induced band splitting. The constant energy section at the Fermi surface depicted in Fig. 6 **a,b** indicates an excellent agreement of experiment and theory. The band dispersion along the Γ - X direction shown in Fig. 6 **c** shows band A crossing the Fermi level and band C at a mean binding energy of 150 meV. The energy distribution curve of the photoemission intensity along the indicated profile [Fig. 6 **g**], crossing the maximum of band C, reveals the occurrence of two separated intensity maxima. The profile can be fitted with three states at 75 meV, 150 meV, and 225 meV, indicating a band splitting of 150 meV. The corresponding calculated profile [Fig. 6 **h**] shows three distinct maxima originating from the overlay of the splitted band with momentum perpendicular to the Néel vector and the degenerate state with momentum along the Néel vector. The calculated binding energies for the three states belonging to band C are 150 meV, 200 meV, and 250 meV, resulting in a maximum band splitting of 100 meV.

The observed anisotropy of the electronic band structure induced by the orientation of the Néel vector can be understood by considering the breaking of inversion symmetry due to antiferromagnetic order. The paramagnetic space group of Mn_2Au is I4/mmm and the two Mn atoms are connected *via* inversion symmetry. Antiferromagnetism in Mn_2Au breaks the inversion symmetry, *i.e.* $E(k)$ does not equal $E(-k)$. However, the Mn atoms are still connected *via* the combined PT-symmetry (spatial inversion P coupled with time-reversal T) and the energy bands of Mn_2Au are thus Kramers degenerate, *i.e.* $E^{\uparrow}(k) = E^{\downarrow}(k)$. To understand how the antiferromagnetic order affects the k-dependence of the electronic structure, we analyze magnetic symmetries and *ab initio* calculated energy bands shown in Fig. 7.

The antiferromagnetic symmetry space group without spin-orbit interaction is P4/m'mm.

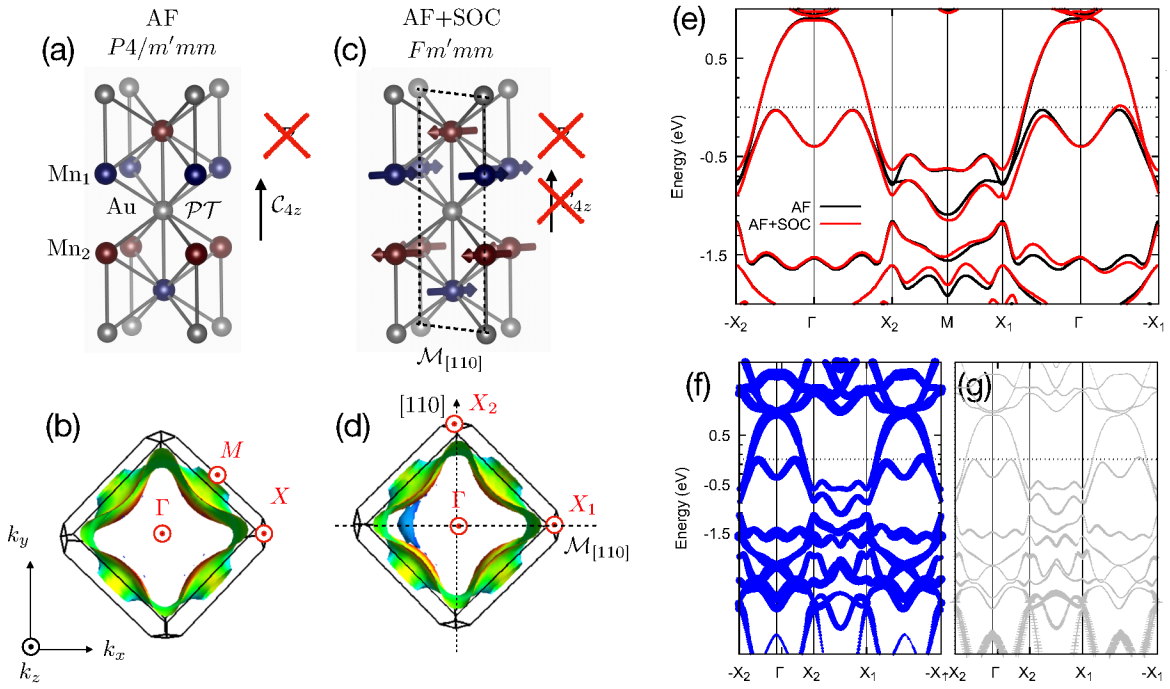

Figure 7: (a) Sketch of the P4/m'mm structure of antiferromagnetic Mn_2Au with magnetic sublattices indicated in red and blue and highlighted combined spatial inversion and time-reversal symmetry PT. (b) Calculated Fermi surface without spin-orbit coupling (SOC). (c) Sketch of the Fm'mm structure with SOC present. (d) Corresponding Fermi surface showing broken C4z and inversion symmetries. Notice the appearance of a hole-type Fermi surface sheet (blue). (e) Calculated band structure without and with SOC. (f) Orbital projection of bands shown in (e) on Mn-located states with localization indicated by the symbol size. (g) Similar data for Au-located states.

This symmetry group includes the C4z rotation since the antiferromagnetic densities are not coupled to the lattice [see Fig. 7(a)]. We illustrate the C4z symmetry also on the calculated Fermi surface cut in Fig. 7(b). Adding on top of antiferromagnetic moments also the spin-orbit interaction reduces the magnetic space group to Fm'mm. In Fig. 7(c,d) we observe that the C4z is broken by the coupling of the moments to the lattice. We note that for the Néel vector along the [110] direction, there is still a mirror plane symmetry M[110]. The corresponding band structure, shown in Fig. 7(e), confirms this conclusion. If we rotate the Néel vector to the $[\bar{1}\bar{1}0]$ direction, the blue hole region in the Fermi surface, shown in Fig. 7(d), will rotate its position to the $-k_x$ position in the Brillouin zone. Since in the experiment we averaged photoemission intensity from both of these domains, we see only the C4z symmetry breaking induced anisotropy. The magnetic inversion symmetry breaking remains hidden in multidomain samples. In Fig. 7(f,g), we show that the energy bands are composed of both Mn and Au states, where the latter is presumably enhancing the spin-orbit induced deformation of the energy bands seen in Fig. 7(e).

The antiferromagnetism in Mn_2Au represents a special type of inversion symmetry breaking, which is different from structural chiral symmetry breaking: it introduces coupling of the energy bands to the Néel vector direction. Thus, antiferromagnetic Mn_2Au exhibits a magnetic toroidal dipole Fermi surface, i. e. a spin degenerate Fermi surface,[37] which is not symmetric around the Γ point. Experimentally, we see the effect of averaging over AFM domains with antiparallel Néel vector.

CONCLUSIONS

We experimentally observed a symmetry breaking of the electronic states of capped $Mn_2Au(001)$ epitaxial thin films induced by the orientation of the Néel vector. This symmetry breaking is already present at the Fermi energy, but is strongest at a binding energy of ≈ 0.2 eV. We observed a maximum asymmetry of ≈ 10 % probed by bulk-sensitive hard X-ray photoemis-

sion spectroscopy (probing depth $\simeq 5$ nm), which is reduced to ≈ 5 % if probing with more surface sensitive soft X-rays (probing depth $\simeq 1$ nm). Additionally, probing uncapped samples even more surface sensitive with vacuum-ultraviolet light reveals a maximum spin-orbit interaction induced band splitting of ≈ 100 meV.

The Néel vector induced breaking of the crystallographic symmetry visible in the photoelectron momentum patterns is consistent with band structure calculations. The antiferromagnetic spectral function calculated using *ab initio* methods shows the same principal changes, if the Néel vector is switched between the two easy axes, which appear non-equivalent when including spin-orbit coupling. We conclude that the combined antiferromagnetic and spin-orbit interaction leads to C4z symmetry breaking, which manifests itself in large anisotropies in the constant energy maps of the electronic states. Experimental and theoretical results reveal an energetic rearrangement of conduction electrons propagating perpendicular to the Néel vector. These anisotropies can lead to large magnetoresistance, transport and topological effects.

METHODS

Epitaxial $Mn_2Au(001)$ thin films with a thickness of 40 nm were deposited by rf sputtering from a stoichiometic target on a Al_2O_3 $(1\bar{1}02)$ substrate with an epitaxial Ta(001) buffer layer as described in Ref.[29] The in-plane epitaxial relation as determined by X-ray diffractometry (XRD) and reflection high energy electron diffraction (RHEED) is Ta(001)[100] $\parallel$ $Mn_2Au(001)$[100]. The XRD rocking curve of the Mn_2Au (002) peak indicates a mosaicity of $\approx 0.5^{o}$. This is relevant for hard X-ray experiments, since this mosaicity translates to a smearing of the parallel momentum of 0.3 $Å^{-1}$ for a photon energy of 5 keV, corresponding to 15 % of the Brillouin zone diameter. The RHEED pattern of the $Mn_2Au(001)$ surface shows an arrangement of spots on semicircles, which is typical for a well ordered smooth surface. The corresponding figures and more details on the sample preparation and characterization can be found in

Refs.[28,29]

For persistent Néel vector alignment, the samples were capped with 2 nm of either Ta, Al, or SiN and exposed to high magnetic fields to generate a spin-flop transition. For the spin-flop transition, pulsed magnetic fields of 60 T were applied along the easy [110]- and [1-10]-direction at 77 K at the High Magnetic Field Laboratory of the Helmholtz-Zentrum Dresden-Rossendorf (HZDR). X-ray magnetic linear dichroism photoemission electron microscopy of the Mn_2Au thin films demonstrated an almost complete resulting alignment of the Néel vector.[30]

We performed the HARPES experiments with one 10×10 mm Ta-capped (2 nm) sample, that was divided in two halves subsequent to the sample preparation and prior to the magnetic field exposure. We applied the magnetic field parallel to the long and short axis of each 5×10 mm half, respectively, which corresponds to perpendicular easy $< 110 >$ directions. For the HARPES experiments, we then reunify the two halves on the sample plate in their original relative position. By this procedure, we exclude any substrate-induced asymmetries originating *e.g.* from the two-fold surface symmetry of the Al_2O_3(1-120) substrate. Additionally, we exclude asymmetries stemming from photoemission linear dichroism by comparing the photoemission intensities from both halves measured in identical geometry.

For the HARPES experiments, the samples are inserted into a He-cooled (25 K) sample stage on a high precision 6-axis hexapod manipulator of the time-of-flight momentum microscope.[26] The HARPES experiments were performed at beamline P22 of the storage ring PETRA III at DESY in Hamburg (Germany). Owing to the high energy (6.0 GeV) and large size (2.3 km circumference) of PETRA, P22 provides hard X-rays with the highest brilliance worldwide in an energy range from 2.4 to 15 keV. Present conditions were 2×10^{13} photons/s at 4-6 keV in a spot of about 10×10 μm^2 using a Si(111) double-crystal monochromator.[27] The bandwidth varies from 350 meV in the 3 keV range to 500 meV at 5 keV for the Si(111) crystal. The Si(311) crystal used for the present experiment yields a three times smaller bandwidth. At 5.3 keV we measured a band width of 155 meV.

A key benefit of angle-resolved photoelectron spectroscopy in the hard X-ray range is the significant increase of the information depth,[38] thanks to the large inelastic mean-free-path of the escaping photoelectrons.[39] In practice, HARPES faces challenges by low cross sections, the Debye-Waller reduction of the coherent spectral fraction, and photoelectron diffraction effects. Phonon scattering destroys the initial momentum distribution and produces a significant background. Subsequent X-ray photoelectron diffraction (XPD) at the lattice imprints a pronounced Kikuchi-type diffraction pattern both on the background signal and on the direct transition photoelectrons.

Extending time-of-flight momentum microscopy into the hard X-ray regime overcomes these challenges. For the examples of the medium-Z element materials Mo and layered $TiTe_2$, it has been demonstrated, how comprehensive valence-band and core-level photoemission data acquired under identical electron optical settings can be used to effectively remove photoelectron diffraction effects in HARPES band dispersions.[27]

Soft X-ray photoemission experiments using conventional angular-resolved photoemission spectroscopy have been performed at the high-resolution soft X-ray beamline ADRESS at the Swiss Light Source for resonant inelastic X-ray scattering and angle-resolved photoelectron spectroscopies.[40,41] The Fermi-level position of ARPES spectra has been determined by a Au foil in electrical contact with the sample. A similar Mn_2Au sample as for the HARPES experiment has been capped by 2 nm SiN and Néel vector oriented in a magnetic field of 50 T prior to the photoemission experiment. The sample has been illuminated with soft X-ray radiation with an incidence angle of 20° with respect to the in-plane magnetic easy axis. Two measurements were done with azimuthal orientation parallel and perpendicular to the Néel vector. The measurements were conducted at a temperature of 12 K, with varying the photon energy from 500 to 1000 eV. The perpendicular moment was adjusted to the Γ point at a photon energy of 817 eV. The total energy resolution including the thermal broadening was 90 meV at $h\nu = 817$ eV. The incident beam has linear-vertical polarization, corresponding to *p*-polarization. The SX-ARPES results shown in Fig. 4 have been similarly

symmetrized as the HARPES data, while data shown in Fig. 5 shows the data as measured.

Momentum microscopy in the vacuum ultraviolet photon energy range has been conducted in our laboratory using a single-hemisphere momentum microscope[42] and a He discharge lamp (21.2 eV) for photon excitation. Uncapped samples have been transferred directly after deposition to the photoemission chamber *via* an ultrahigh vacuum suitcase. Hence, the as grown samples comprise domains with Néel vector orientation equally distributed parallel to both magnetic easy axes. The total energy resolution of this experiment performed at a sample temperature of 10 K is set by the pass energy and entrance slit to 50 meV. The VUV-ARPES results shown in this article have also been symmetrized as in the case of the HARPES.

The experimental results were compared with calculations based on *ab initio* spin-density functional theory with local-density approximation. The spectral function of $Mn_2Au(001)$ was computed for an infinite system using the fully relativistic Korringa-Kohn-Rostoker method as implemented in the Munich SPR-KKR package.[43,44] Theoretical results for the Néel vector being aligned parallel to the [110] and [-1-10] directions were averaged to reflect the experimental situation, where the field alignment results in an equal distribution of both antiparallel directions.

For the equilibrium density functional theory calculations and symmetry analysis shown in Fig.7, we used the FLAPW code ELK. We used the BCT unit cell and a k-point mesh $10 \times 10 \times 10$. We plot the Fermi surfaces with the program Fermisurfer.[45]

Author Contributions

H.J.E., M.J., L.S. and G.S. wrote the paper. S.V.C. and H.J.E. performed the data evaluation. H.J.E., S.V.C., S.P.B., K.M., S.B., O.F., D.V., S.Y.A., and G.S. set up and carried out the HARPES experiment. M.J., V.S. and H.J.E. conducted the SX-ARPES experiment. S.P.B. and S.Yu.B. prepared and characterized the Mn_2Au samples. Y.S. performed the high

field application. C.S., A.G., and Yu.M. helped with the beamline and microscopy control unit at DESY. S.W.D. and J.M. performed *ab initio* calculations. L.S. and J.S. analysed the magnetic symmetries and performed and analysed *ab initio* calculations. M.J. and H.J.E. coordinated the project. All authors discussed the results and contributed to the writing of the manuscript.

Acknowledgement

This work was funded by the Deutsche Forschungsgemeinschaft (DFG, German Research Foundation) Grant No. TRR 173 268565370 (projects A01, A03, and A05) and by the BMBF (projects 05K16UM1 and 05K19UM2). S. W. D. and J. M. would like to thank CEDAMNF project financed by the Ministry of Education, Youth and Sports of Czech Republic, Project No. CZ.02.1.01/0.0/0.0/15.003/0000358) and also for the support by the GAČR *via* the project 20-18725S. We acknowledge the support of the HLD at HZDR, member of the European Magnetic Field Laboratory (EMFL). We acknowledge the Paul Scherrer Institut, Villigen, Switzerland for provision of synchrotron radiation beamtime at the soft-X-ray ARPES endstation of beamline ADRESS of the SLS. Sincere thanks are due to A. Oelsner (Surface Concept GmbH) for continuous support and to N. Schroeter for his help setting up the vacuum suitcase at ADRESS.

References

1. MacDonald, A. H.; Tsoi, M. Antiferromagnetic Metal Spintronics. Philos. Trans. Royal Soc. A **2011**, 369, 3098.

2. Park, B. G.; Wunderlich, J.; Marti, X.; Holy, V.; Kurosaki, Y.; Yamada, M.; Yamamoto, H.; Nishide, A.; Hayakawa, J.; Takahashi, H.; Shick, A. B.; Jungwirth, T.

A Spin-Valve-Like Magnetoresistance of an Antiferromagnet-Based Tunnel Junction. Nature Materials **2011**, 10, 347.

3. Gomonay, E. V.; Loktev, V. M. Spintronics of Antiferromagnetic Systems. Low. Temp. Phys. **2014**, 40, 17.

4. Jungwirth, T.; Marti, X.; Wadley, P.; Wunderlich, J. Antiferromagnetic Sspintronics. Nat. Nanotech. **2016**, 11, 231.

5. Gomonay, O.; Jungwirth, T.; Sinova, J. Concepts of Antiferromagnetic Spintronics. Phys. Stat. Sol. RRL **2017**, 11, 1700022.

6. Baltz, V.; Manchon, A.; Tsoi, M.; Moriyama, T.; Ono, T.; Tserkovnyak, Y. Antiferromagnetic Spintronics. Rev. Mod. Phys. **2018**, 90, 015005.

7. Zelezny, J.; Gao, H.; Vyborny, K.; Zemen, J.; Masek, J.; Manchon, A.; Wunderlich, J.; Sinova, J.; Jungwirth, T. Relativistic Neel-Order Fields Induced by Electrical Current in Antiferromagnets. Phys. Rev. Lett. **2014**, 113, 157201.

8. Wadley, P.; Howells, B.; Zelezny, J.; Andrews, C.; Hills, V.; Campion, R. P.; Novak, V.; Olejnik, K.; Maccherozzi, F.; Dhesi, S. S.; Martin, S. Y.; Wagner, T.; Wunderlich, J.; Freimuth, F.; Mokrousov, Y.; Kunes, J.; Chauhan, J. S.; Grzybowski, M. J.; Rushforth, A. W.; Edmonds, K. W. *et al.* Electrical Switching of an Antiferromagnet. Science **2016**, 351, 587.

9. Grzybowski, M. J.; Wadley, P.; Edmonds, K. W.; Beardsley, R.; Hills, V.; Campion, R. P.; Gallagher, B. L.; Chauhan, J. S.; Novak, V.; Jungwirth, T.; Maccherozzi, F.; Dhesi, S. S. Imaging Current-Induced Switching of Antiferromagnetic Domains in CuMnAs. Phys. Rev. Lett. **2017**, 118, 057701.

10. Wadley, P.; Reimers, S.; Grzybowski, M. J.; Andrews, C.; Wang, M.; Chauhan, J. S.; Gallagher, B. L.; Campion, R. P.; Edmonds, K. W.; Dhesi, S. S.; Maccherozzi, F.;

Novak, V.; Wunderlich, J.; Jungwirth, T. Current Polarity-Dependent Manipulation of Antiferromagnetic Domains. Nat. Nanotech. **2018**, 13, 362.

11. Bodnar, S. Y.; Smejkal, L.; Turek, I.; Jungwirth, T.; Gomonay, O.; Sinova, J.; Sapozhnik, A. A.; Elmers, H. J.; Kläui, M.; Jourdan, M. Writing and Reading Antiferromagnetic Mn_2Au by Néel Spin-Orbit Torques and Large Anisotropic Magnetoresistance. Nat. Comm. **2018**, 9, 348.

12. Meinert, M.; Graulich, D.; Matalla-Wagner, T. Electrical Switching of Antiferromagnetic Mn_2Au and the Role of Thermal Activation. Phys. Rev. Appl. **2018**, 9, 064040.

13. Arana, M.; Gamino, M.; Silva, E. F.; Barthem, V. M. T. S.; Givord, D.; Azevedo, A.; Rezende, S. M. Spin to Charge Current Conversion by the Inverse Spin Hall Effect in the Metallic Antiferromagnet Mn_2Au at Room Temperature. Phys. Rev. B **2018**, 98, 144431.

14. Chen, X.; Zhou, X.; Cheng, R.; Song, C.; Zhang, J.; Wu, Y.; Ba, Y.; Li, H.; Sun, Y.; You, Y.; Zhao, Y.; Pan, F. Electric Field Control of Néel Spin-Orbit Torque in an Antiferromagnet. Nat. Materials **2019**, 18, 931.

15. Bodnar, S. Y.; Filianina, M.; Bommanaboyena, S. P.; Forrest, T.; Maccherozzi, F.; Sapozhnik, A. A.; Skourski, M., Y. Kläui; Jourdan, M. Imaging of Current Induced Néel Vector Switching in Antiferromagnetic Mn_2Au. Phys. Rev. B **2019**, 99, 140409(R).

16. Kokado, S.; Tsunoda, M.; Harigaya, K.; Sakuma, A. Anisotropic Magnetoresistance Effects in Fe, Co, Ni, Fe_4N, and Half-Metallic Ferromagnet: A Systematic Analysis. J. Phys. Soc. Jap. **2012**, 81, 024705.

17. Bodnar, S.; Skourski, Y.; Gomonay, O.; Sinova, J.; Kläui, M.; Jourdan, M. Magnetoresistance Effects in the Metallic Antiferromagnet Mn_2Au. Phys. Rev. Appl. **2020**, 14, 014004.

18. Bhatti, S.; Sbiaa, R.; Hirohata, A.; Ohno, H.; Fukami, S.; Piramanayagam, S. N. Spintronics Based Random Access Memory: A Review. Materials Today **2017**, 20, 530.

19. Fang, Z.; Nagaosa, N.; Takahashi, K.; Asamitsu, A.; Mathieu, R.; Ogasawara, T.; Yamada, H.; Kawasaki, M.; Tokura, Y.; Terakura, K. The Anomalous Hall Effect and Magnetic Monopoles in Momentum Space. Science **2003**, 302, 92.

20. Yao, Y.; Kleinman, L.; MacDonald, A.; Sinova, J.; Jungwirth, T.; Wang, D.; Wang, E.; Niu, Q. First Principles Calculation of Anomalous Hall Conductivity in Ferromagnetic bcc Fe. Phys. Rev. Lett. **2004**, 92, 037204.

21. Berger, L. Influence of Spin-Orbit Interaction on the Transport Processes in Ferromagnetic Nickel Alloys in the Presence of a Degeneracy of the 3D Band. Physica **1964**, 30, 1141.

22. van der Laan, G. Microscopic Origin of Magnetocrystalline Anisotropy in Transition Metal Thin Films. J. Phys. Condens. Matter **1998**, 10, 3239.

23. Mlynczak, E.; Eschbach, M.; Borek, S.; Minar, J.; Braun, J.; Aguilera, I.; Bihlmayer, G.; Doring, S.; Gehlmann, M.; Gospodaric, P.; Suga, S.; Plucinski, L.; Blugel, S.; Ebert, H.; Schneider, C. M. Fermi Surface Manipulation by External Magnetic Field Demonstrated for a Prototypical Ferromagnet. Phys. Rev. X **2016**, 6, 041048.

24. Schulz, S.; Nechaev, I. A.; Guettler, M.; Poelchen, G.; Generalov, A.; Danzenbaecher, S.; Chikina, A.; Seiro, S.; Kliemt, K.; Vyazovskaya, A. Y.; Kim, T. K.; Dudin, P.; Chulkov, E. V.; Laubschat, C.; Krasovskii, E. E.; Geibel, C.; Krellner, C.; Kummer, K.; Vyalikh, D. V. Emerging 2D-Ferromagnetism and Strong Spin-Orbit Coupling at the Surface of Valence-Fluctuating $EuIr_2Si_2$. npj Quantum Materials **2019**, 4, 26.

25. Smejkal, L.; Zelezny, J.; Sinova, J.; Jungwirth, T. Electric Control of Dirac Quasiparticles by Spin-Orbit Torque in an Antiferromagnet. Phys. Rev. Lett. **2017**, 118, 106402.

26. Medjanik, K.; Babenkov, S. V.; Chernov, S.; Vasilyev, D.; Schönhense, B.; Schlueter, C.; Gloskovskii, A.; Matveyev, Y.; Drube, W.; Elmers, H. J.; Schönhense, G. Progress in HAXPES Performance Combining Full-Field k-Imaging with Time-of-Flight Recording. J. Synchrotron Rad. **2019**, 26, 1996.

27. Babenkov, S.; Medjanik, K.; Vasilyev, D.; Chernov, S.; Schlueter, C.; Gloskovskii, A.; Matveyev, Y.; Drube, W.; Schonhense, B.; Rossnagel, K.; Elmers, H. J.; Schönhense, G. High-Accuracy Bulk Electronic Bandmapping with Eliminated Diffraction Effects Using Hard X-Ray Photoelectron Momentum Microscopy. Comm. Phys. **2019**, 2, 107.

28. Jourdan, M.; Braeuning, H.; Sapozhnik, A.; Elmers, H. J.; Zabel, H.; Klaeui, M. Epitaxial Mn_2Au Thin Films for Antiferromagnetic Spintronics. J. Phys. D: Appl. Phys. **2015**, 48, 385001.

29. Bohammaboyena, S. P.; Bergfeldt, T.; Heller, R.; Kläui, M.; Jourdan, M. High Quality Epitaxial Mn_2Au (001) Thin Films Grown by Molecular Beam Epitaxy. J. Appl. Phys. **2020**, 127, 243901.

30. Sapozhnik, A. A.; Filianina, M.; Bodnar, S. Y.; Lamirand, A.; Mawass, M.-A.; Skourski, Y.; Elmers, H.-J.; Zabel, H.; Klaeui, M.; Jourdan, M. Direct Imaging of Antiferromagnetic Domains in Mn_2Au Manipulated by High Magnetic Fields. Phys. Rev. B **2018**, 97, 134429.

31. Sapozhnik, A. A.; Abrudan, R.; Skourski, Y.; Jourdan, M.; Zabel, H.; Klaeui, M.; Elmers, H. J. Manipulation of Antiferromagnetic Domain Distribution in Mn2Au by Ultrahigh Magnetic Fields and by Strain. Phys. Stat. Sol. Rapid Res. Lett. **2017**, 11, 1600438.

32. Tanuma, S.; Powell, C. J.; Penn, D. R. Calculations of Electron Inelastic Mean Free Paths. IX. Data for 41 Elemental Solids over the 50 eV to 30 keV Range. Surf. Interface Anal. **2011**, 43, 689.

33. Setyawan, W.; Curtarolo, S. High-Throuput Electronic Band Structure Calculations. Challenges and tools Comp. Mat. Sci. **2010**, 49, 299.

34. Hüfner, S. Photoelectron Spectroscopy - Principles and Applications; Springer: Berlin, 2003.

35. Reinert, F.; Hüfner, S. Photoemission Spectroscopy–from Early Days to Recent Applications. New J. Phys. **2005**, 7, 97.

36. Schönhense, G.; Medjanik, K.; Babenkov, S.; Vasilyev, D.; Ellguth, M.; Fedchenko, O.; Chernov, S.; Schönhense, B.; Elmers, H. J. Momentum-Transfer Model of Valence-Band Photoelectron Diffraction. Comm. Phys. **2020**, 3, 45.

37. Hayami, S.; Yatsushiro, M.; Yanagi, Y.; Kusunose, H. Classification of Atomic-Scale Multipoles under Crystallographic Point Groups and Application to Linear Response Tensors. Phys. Rev. B **2018**, 98, 165110.

38. Gray, A. X.; Papp, C.; Ueda, S.; Balke, B.; Yamashita, Y.; Plucinski, L.; Minar, J.; Braun, J.; Ylvisaker, E. R.; Schneider, C. M.; Pickett, W. E.; Ebert, H.; Kobayashi, K.; Fadley, C. S. Probing Bulk Electronic Structure with Hard X-Ray Angle-Resolved Photoemission. Nat. Materials **2011**, 10, 759.

39. Kobayashi, K. High-Resolution Hard X-Ray Photoelectron Spectroscopy: Application of Valence Band and Core-Level Spectroscopy to Materials Science. Nucl. Instrum. Methods Phys. Res. A **2005**, 547, 98.

40. Strocov, V. N.; Schmitt, T.; Flechsig, U.; Schmidt, T.; Imhof, A.; Chen, Q.; Raabe, J.; Betemps, R.; Zimoch, D.; Krempasky, J.; Wang, X.; Grioni, M.; Piazzalunga, A.; Patthey, L. High-Resolution Soft X-Ray Beamline ADRESS at the Swiss Light Source for Resonant Inelastic X-Ray Scattering and Angle-Resolved Photoelectron Spectroscopies. J. Synchr. Rad. **2010**, 17, 631.

41. Strocov, V. N.; Wang, X.; Shi, M.; Kobayashi, M.; Krempasky, J.; Hess, C.; Schmitt, T.; Patthey, L. Soft-X-Ray ARPES Facility at the ADRESS Beamline of the SLS: Concepts, Technical Realisation and Scientific Applications. J. Synchrotron Rad. **2014**, 21, 32.

42. Schönhense, G.; Babenkov, S.; Vasilyev, D.; Elmers, H. J.; Medjanik, K. Single-Hemisphere Photoelectron Momentum Microscope With Time-of-Flight Recording. **2020**, 2007.16095v2. arXiv. https://arxiv.org/abs/2007.16095v2 (accessed November 17, 2020).

43. Ebert, H. *The Munich SPR-KKR package*, version 7.7. http://olymp.cup.uni-muenchen.de/ak/ebert/SPRKKR, 2017.

44. Ebert, H.; Koedderitzsch, D.; Minar, J. Calculating Condensed Matter Properties Using the KKR-Greens Function Method-Recent Developments and Applications. Rep. Prog. Phys. **2011**, 74, 096501.

45. Kawamura, M. FermiSurfer: Fermi-Surface Viewer Providing Multiple Representation Schemes. Comp. Phys. Comm. **2019**, 239, 197.